was excellent for subjective image noise, pixellated blotchy appearance and diagnostic acceptability (κ=0.80–1.00). Intraobserver agreement was variable for motion artefacts (κ=0.35 for reader 1 and κ=0.51 for reader 2) and streak artefacts (κ=0.96 for reader 1 and κ=0.67 for reader 2).

Subjective image noise, image artefacts and diagnostic acceptability with MBIR and ASIR techniques are summarised in Table 5 (also see Appendix 3 for details of subjective scores). For subjective image noise, modal scores were "less than average" for low-dose MBIR and "average" for reference-dose ASIR ($P<0.001$ for both readers). None of the low-dose MBIR images was graded with "substantial" or "unacceptable image noise". Conversely, low-dose ASIR images were typically associated with "substantial" or "unacceptable image noise" ($P<0.001$ each vs. the other two image data sets for both readers). For diagnostic acceptability, modal scores were "fully acceptable" or "probably acceptable" for low-dose MBIR and "fully acceptable" for reference-dose ASIR ($P<0.001$ for reader 2). There were no "diagnostically unacceptable" low-dose MBIR images, whereas low-dose ASIR images were typically graded as "diagnostically unacceptable" ($P<0.001$ each vs. the other two image data sets for both readers).

While streak artefacts were unapparent or minimally recognisable in most reference-dose ASIR images, streak artefacts not affecting diagnostic interpretation were noted in some low-dose MBIR images, with variability between readers ($P>0.90$ for reader 1 and $P=0.0023$ for reader 2). Low-dose MBIR images were also more often associated with motion artefacts and pixellated blotchy appearance compared with ASIR images ($P<0.001$ for both readers). However, neither of the artefacts affected diagnostic interpretation.

Pixellated blotchy appearance resulted in a step-like appearance at the tissue interfaces and notably affected the sharp visualisation of the following anatomical structures in low-dose MBIR images: pulmonary fissures (13/100 for reader 1, 18/100 for reader 2; $P<0.001$ each vs. reference- and low-dose ASIR for reader 2), the small peripheral lung vessel walls and bronchus (8/100 for reader 1, 1/100 for reader 2; $P<0.001$ each vs. reference- and low-dose ASIR for reader 1) and the border between the pleura and the thoracic wall (84/100 for reader 1, 7/100 for reader 2; $P<0.001$ each vs. reference- and low-dose ASIR for both readers).

MTF estimation

Results of the estimation of the MTF, or spatial resolution, are summarised in Fig. 3. There was consistent improvement both at the iso-centre and off centre in the spatial resolution of images reconstructed with MBIR compared with the ASIR and the FBP images at 5 %, 10 % and 50 % MTF.

Discussion

In this prospective study of 100 patients, image quality characteristics of low-dose chest CT reconstructed with MBIR and ASIR, and reference-dose chest CT reconstructed with ASIR were compared. In chest CT images acquired with nearly 80 % less radiation (low-dose CT), significant improvements in image noise and streak artefacts were observed with the use of MBIR compared with ASIR. Low-dose CT images obtained using MBIR were diagnostically acceptable. To the best of our knowledge, this is the first prospective clinical study to evaluate CT radiation dose reduction in the same patients and compare image quality characteristics with two different reconstruction methods, MBIR and ASIR.

For low-dose CT, MBIR significantly improved objective image noise in the lung parenchyma compared with ASIR.

Table 5 Subjective image quality scores for the two radiologists (reader 1 and reader 2)

Image quality	Reader 1			Reader 2		
	Reference-dose ASIR	Low-dose ASIR	Low-dose MBIR	Reference-dose ASIR	Low-dose ASIR	Low-dose MBIR
Noise (1/2/3/4/5)	0/0/99/1/0*	0/1/5/59/5*	0/100/0/0/0*	0/1/98/1/0*	0/1/8/61/30*	8/75/17/0/0*
Motion artefact (1/2/3)	96/4/0‡	95/5/0‡	77/23/0‡	94/6/0‡	95/4/1‡	58/38/4‡
Streak artefact (1/2/3)	99/1/0†	6/12/82†	98/2/0†	97/2/1**	27/67/6**	83/16/1**
Pixellated blotchy appearance (1/2/3)	100/0/0‡‡	99/1/0‡‡	1/99/0‡‡	100/0/0‡‡	99/1/0‡‡	4/96/0‡‡
Diagnostic acceptability (1/2/3/4)	99/1/0/0††	6/10/49/35††	94/6/0/0††	97/2/1/0 ***	8/13/49/30***	41/53/6/0***

Data show the frequency of numerical scores given in each category for the 100 patients. Using a sign test, the subjective score differences were statistically significant between all pairs in image noise for both readers (*$P<0.001$), in streak artefacts for reader 2 (**$P<0.003$) and in diagnostic acceptability for reader 2 (***$P<0.001$). The subjective score differences of low-dose ASIR vs. reference-dose ASIR, and low-dose ASIR vs. low-dose MBIR were significant with regard to streak artefacts for reader 1 ($^{\dagger}P<0.001$) and in diagnostic acceptability for reader 1 ($^{\dagger\dagger}P<0.001$). The subjective score differences of low-dose MBIR vs. reference-dose ASIR, and low-dose MBIR vs. low-dose ASIR were significant with regard to motion artefacts for both readers ($^{\ddagger}P<0.001$), and in pixellated blotchy appearance for both readers ($^{\ddagger\ddagger}P<0.001$)

Compared with reference-dose ASIR, objective image noise in the lung parenchyma was significantly lower with low-dose MBIR than with reference-dose ASIR; however, the results were the opposite in the descending aorta. This may be for the following reason: it is acknowledged that reconstruction kernels used for FBP images can largely influence objective image noise in FBP and subsequently in ASIR-FBP-blended images (50 %/50 % blending was used in the present study). High-pass filter algorithms preserve the higher spatial frequencies at the expense of greater noise, whereas low-pass filter algorithms reduce the higher frequency contribution, which decreases noise but also degrades spatial resolution. The chest kernel used in the present study is equivalent to a high-pass filter algorithm (e.g. the lung kernel) for depiction of the lung and is equivalent to a low-pass filter algorithm (e.g. the soft-tissue kernel) for depiction of the mediastinal soft tissue [21, 22]. Therefore, the mixed results between the lung parenchyma and the aorta for objective image noise can be largely explained by the reconstruction kernel.

Image features uniquely noted in the MBIR-reconstructed images in the present study included motion artefacts and a pixellated blotchy appearance. The reason why there are greater motion artefacts with MBIR than with ASIR images is not clear; however, it may be due to differences in time resolution between MBIR and ASIR, and needs to be fully investigated in future studies. The exact reasons for the pixellated blotchy appearance uniquely seen on MBIR are also unknown; inherent differences in image reconstruction may have contributed to these differences. One can argue that the pixellated blotchy appearance may be ascribed to lower spatial resolution; however, our phantom study shows consistent improvement in the spatial resolution of images reconstructed with MBIR compared with the ASIR (Fig. 3). A pixellated blotchy appearance has been described in many initial ASIR reports [9, 14–17]. However, this appearance was not prominently seen on ASIR images in the present study, which, according to the vendor, can be attributed to the advancements of the ASIR algorithm that have been made following the earlier studies. A pixellated blotchy appearance on MBIR images resulted in a step-like appearance at the tissue interfaces and affected the sharp visualistion of some anatomical structures (rated "not sharply visualised"), such as the pulmonary fissures, small pulmonary vessels and bronchi, and the border between the pleura and the thoracic wall. Overall, these MBIR-unique image features were not overly distracting in the present study and had little effect on diagnostic acceptability. However, the difference in image appearance and lack of reader familiarity may have contributed to the variability between the readers, particularly in the subjective evaluation of some image artefacts and anatomical structures. This variability should decrease over the course of familiarisation with MBIR images and may decrease even more if the MBIR-unique image appearance becomes less prominent with further advancement of the MBIR algorithm.

The radiation dose delivered by low-dose CT in the present study was almost equivalent to the dose described in NLST [24]. As the present results indicate that MBIR has a greater potential than ASIR to provide diagnostically acceptable low-dose CT images without severely compromising image quality, MBIR is expected to be helpful particularly in certain patients and settings, such as imaging infants and young patients or screening for lung cancer. The ability of MBIR to detect and localise lesions not only in the chest but also in different body regions needs to be investigated in further clinical studies. Although not assessed in the present study, the behaviour of MBIR concerning image noise at increased slice thicknesses (e.g. 2.5–5 mm) and in coronal/sagittal reformats, which may be used by many radiologists for clinical work, needs to be further investigated in clinical studies. The influence of other dose-reduction techniques such as reducing tube voltage on MBIR should also be assessed in future studies. Another issue to consider for MBIR in a practical setting is the long reconstruction time. Although recent advances have reduced this time to about 1 h per case (the reconstruction time in the present report was not recorded as it was not a feature in the application software), MBIR may not yet be suitable for evaluation in acute clinical settings.

Several limitations of this study must be considered. First, all of the chest CT examinations were performed without intravenous contrast medium administration. The presence of streak artefacts from the superior vena cava is one important issue that needs to be considered in contrast-enhanced chest CT images, and the performance of MBIR with regard to these streaks should be fully investigated in future studies. Second, although MBIR is expected to be helpful in low-dose CT for paediatric patients, patients under the age of 18 were not included in the study. Third, the body size of the patients in this study was generally small. MBIR has not yet been assessed in extremely large or obese patients, and this needs to be investigated in future studies. A fourth limitation of the study is that the results may not apply to other similar iterative reconstruction methods available from other vendors; fifth, owing to the difference in image appearance, blinding of the radiologists between MBIR and ASIR during subjective image analysis was difficult. However, we randomised the image sets acquired with different dose levels and reconstruction techniques.

In conclusion, chest CT images acceptable for diagnostic interpretation acquired with nearly 80 % less radiation can be obtained with the use of MBIR. MBIR

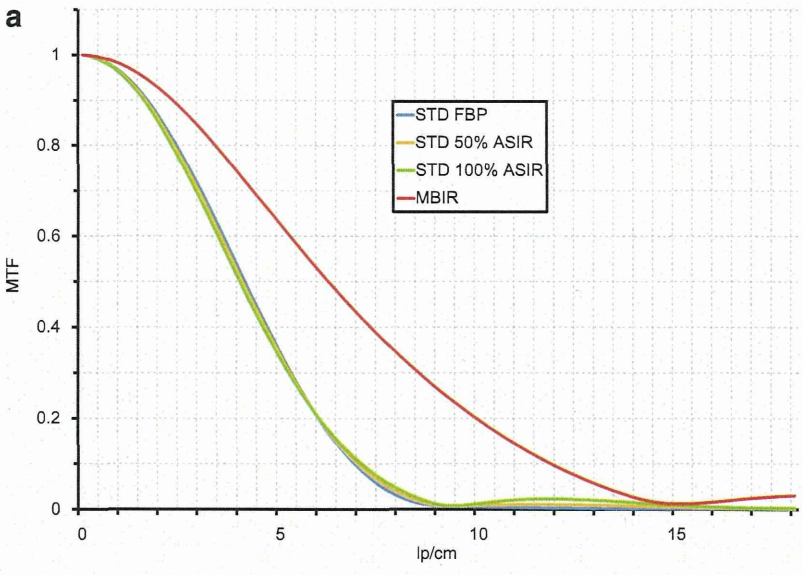

	STD FBP	STD 50% ASIR	STD 100% ASIR	MBIR
50% MTF (lp/cm)	4.12	4.05	3.99	6.40
10% MTF (lp/cm)	6.86	6.94	7.04	11.81
5% MTF (lp/cm)	7.54	7.68	7.86	13.04

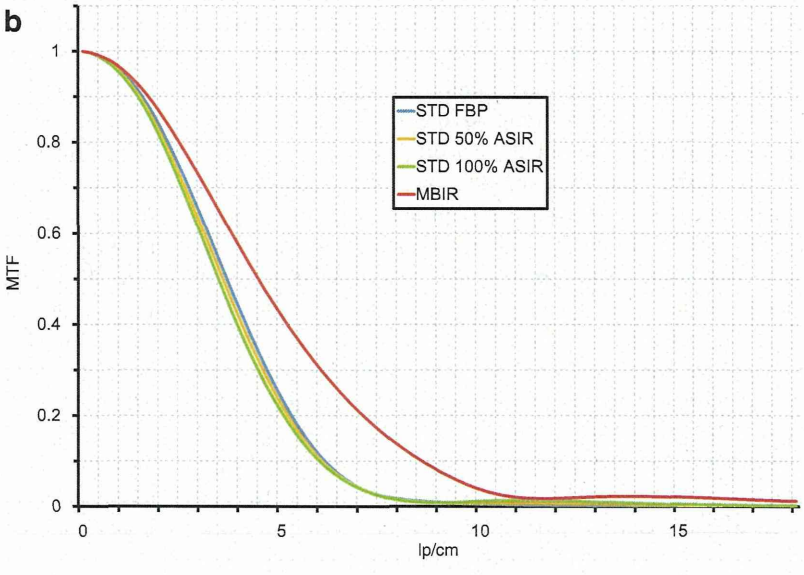

	STD FBP	STD 50% ASIR	STD 100% ASIR	MBIR
50% MTF (lp/cm)	3.62	3.52	3.41	4.41
10% MTF (lp/cm)	6.07	6.00	5.93	8.50
5% MTF (lp/cm)	6.76	6.72	6.69	9.58

Fig. 3 Line graph summarises modulation transfer function (MTF) at the iso-centre (a) and at 10 cm off centre (b) for 0.625-mm images CT reconstructed with filtered back projection (FBP), ASIR (50 % and 100 %) and MBIR. Compared with the ASIR and FBP images, MBIR images had higher spatial resolution at 5 %, 10 % and 50 % MTF. lp/cm=Line pairs per centimetre, STD=standard kernel

shows greater potential than ASIR for providing diagnostically acceptable low-dose CT images without severely compromising image quality. MBIR is expected to be helpful for dose reduction, particularly in certain patients and settings, such as imaging of infants and young patients and screening for lung cancer.

Acknowledgements We gratefully acknowledge Kosuke Sasaki, M.S., and Koji Segawa, R.T., for their technical support and assistance in data acquisition.

Appendix 1

ASIR and MBIR are new iterative reconstruction (IR) algorithms. Unlike the conventional FBP, which is based on simpler mathematical assumptions of the tomographic imaging system, IR generates a set of synthesised projections by accurately modelling the data collection process in CT. The model incorporates statistical system information (including photon statistics and electronic noise in the data acquisition system) and details of the system optics (including the size of each detector cell, dimensions of the focal spot, and the shape and size of each image voxel). The synthesised image is mathematically compared and corrected with the actual measurement in order to adjust estimation of the object's image. The technique then iterates this comparison and correction step in order to achieve close proximity between actual and measured projections. Inconsistencies in the projection measurement due to limited photon statistics and electronic noise are corrected with multiple iterations. These data-processing steps help to improve image quality from the noise and resolution perspectives, but prolong the reconstruction duration compared with FBP because of the intensive computations particularly required for incorporating system optics information.

The ASIR technique models just the photons and electronic noise statistics that primarily affect image noise, which are not as computationally intensive or time-consuming. This enables near real-time display of images at the time of imaging. ASIR also differs from other IR techniques in that the vendor provides a blending tool to blend the FBP with the ASIR images. This is accomplished by reconstruction of CT raw data with both FBP and ASIR techniques and then performing a weighted summation of each data set for the final reconstructed images. Prior phantom and clinical studies have already shown that ASIR provides diagnostically acceptable images with a reduction in image noise for low-radiation dose CT compared with the FBP algorithm [9–18].

The MBIR technique, on the other hand, is a pure IR technique that does not involve blending with FBP images, and is mathematically more complex and accurate than ASIR. MBIR not only incorporates modelling of photon and noise statistics like ASIR, it also involves modelling of system optics. This is unlike ASIR, which uses an idealised set of system optics (as does FBP), resulting in similar data utilisation per image. MBIR analyses the x-ray beam at the focal spot, then as it passes through the patient's body and again as it strikes the detector. The algorithm weights each data point so that noisy projections have less influence on the final results, and this allows more accurate image reconstruction. Phantom experiments have shown that MBIR has the potential to further reduce image noise, improve spatial resolution and thereby allow further dose reduction without compromising image quality [19]. With incorporation of system optics information and therefore a more accurate account of voxel and focal spot size and geometry, one can expect improvements in spatial resolution [19, 20]. Because MBIR is a complicated algorithm, using multiple iterations and multiple models, the reconstruction time is significantly longer than FBP as well as the other IR techniques, even with dedicated state-of-the-art parallel processors. The reconstruction time in the present study was about 1 h per case, although the exact time was not recorded as it was not a feature of the application software.

Appendix 2

The rationale for the NI setting in the present study is as follows. As the specified slice thickness for a given NI setting decreases by a factor of x, maintenance of the same radiation dose requires an increase in NI by a factor of 1 divided by the square root of x. According to the previous radiology literature [13, 23], the NI of 15.75 at a slice thickness of 2.5 mm has been used for reference-dose chest CT. Multiplying 15.75 by the square root of 4 (= 2.5/0.625) results in 31.5. Theoretically, the fixed NI of 31.5 at 0.625 mm should achieve the same radiation dose for reference-dose chest CT from the previous radiology literature. As for the NI setting for low-dose CT, we referred to the average ED for low-dose CT described in the National Lung Screening Trial (NLST, 1.5 mSv) [24], which is about one fifth of the radiation dose for reference-dose chest CT described in the previous radiology literature [13, 23]. As the radiation dose decreases by 1/y, the image noise increases by the square root of y. Multiplying the NI for reference-dose CT in the present study (= 31.5) by the square root of 5 results in an NI of 70.44.

Appendix 3

Subjective image noise was defined as overall graininess or mottle in the lung parenchyma, and was assessed in the lung window setting on a five-point scale (1=no or only minimal image noise, 2=less than average image noise, 3=average image noise, 4=more than average or substantial image noise that may interfere with diagnostic decision-making in less than half of the lung parenchyma, and 5=more than

average or substantial image noise that may interfere with diagnostic decision-making in more than half of the lung parenchyma). Artefacts were graded on a three-point scale (1=artefacts unapparent or only minimally recognisable, 2=artefacts recognised but not interfering with diagnostic decision-making, and 3=substantial artefacts recognised affecting diagnostic decision-making). The following artefacts were assessed: streak artefacts, motion artefacts due to heart wall motion and blotchy pixellated appearance at the tissue interface (Fig. 2b). Critical reproduction of visually sharp anatomical structures was assessed. The following anatomical structures were evaluated: pulmonary fissures; secondary pulmonary lobular structures such as interlobular arteries; large- and medium-sized pulmonary vessels; small pulmonary vessels; large- and medium-sized bronchi; small bronchi; the pleuromediastinal border; the border between the pleura and the thoracic wall; the thoracic aorta; anterior mediastinal structures including thymic residue; the trachea and main bronchi; paratracheal tissue; the carina and lymph node area; and the oesophagus. Diagnostic acceptability was assessed on a four-point scale (1=fully acceptable, 2=probably acceptable, 3=deemed acceptable only for limited clinical conditions, and 4=unacceptable).

References

1. Brenner DJ, Hall EJ (2007) Computed tomography—an increasing source of radiation exposure. N Engl J Med 357:2277–2284
2. Schauer DA, Linton OW (2009) NCRP report no. 160, ionizing radiation exposure of the population of the United States, medical exposure—are we doing less with more, and is there a role for health physicists? Health Phys 97:1–5
3. Amis ES Jr, Butler PF, Applegate KE et al (2007) American College of Radiology white paper on radiation dose in medicine. J Am Coll Radiol 4:272–284
4. Mettler FA Jr, Bhargavan M, Faulkner K et al (2009) Radiologic and nuclear medicine studies in the United States and worldwide: Frequency, radiation dose, and comparison with other radiation sources – 1950–2007. Radiology 253:520–531
5. Kalra MK, Maher MM, Toth TL et al (2004) Strategies for CT radiation dose optimization. Radiology 230:619–628
6. Heyer CM, Mohr PS, Lemburg SP, Peters SA, Nicolas V (2007) Image quality and radiation exposure at pulmonary CT angiography with 100- or 120-kVp protocol: Prospective randomized study. Radiology 245:577–583
7. Diel J, Perlmutter S, Venkataramanan N, Mueller R, Lane MJ, Katz DS (2000) Unenhanced helical CT using increased pitch for suspected renal colic: An effective technique for radiation dose reduction? J Comput Assist Tomogr 24:795–801
8. Kalra MK, Maher MM, Sahani DV et al (2003) Low-dose CT of the abdomen: Evaluation of image improvement with use of noise reduction filters pilot study. Radiology 228:251–256
9. Hara AK, Paden RG, Silva AC, Kujak JL, Lawder HJ, Pavlicek W (2009) Iterative reconstruction technique for reducing body radiation dose at CT: Feasibility study. AJR Am J Roentgenol 193:764–771
10. Flicek KT, Hara AK, Silva AC, Wu Q, Peter MB, Johnson CD (2010) Reducing the radiation dose for CT colonography using adaptive statistical iterative reconstruction: A pilot study. AJR Am J Roentgenol 195:126–131
11. Leipsic J, Labounty TM, Heilbron B et al (2010) Adaptive statistical iterative reconstruction: Assessment of image noise and image quality in coronary CT angiography. AJR Am J Roentgenol 195:649–654
12. Leipsic J, Nguyen G, Brown J, Sin D, Mayo JR (2010) A prospective evaluation of dose reduction and image quality in chest CT using adaptive statistical iterative reconstruction. AJR Am J Roentgenol 195:1095–1099
13. Prakash P, Kalra MK, Digumarthy SR et al (2010) Radiation dose reduction with chest computed tomography using adaptive statistical iterative reconstruction technique: Initial experience. J Comput Assist Tomogr 34:40–45
14. Prakash P, Kalra MK, Kambadakone AK et al (2010) Reducing abdominal CT radiation dose with adaptive statistical iterative reconstruction technique. Invest Radiol 45:202–210
15. Sagara Y, Hara AK, Pavlicek W, Silva AC, Paden RG, Wu Q (2010) Abdominal CT: Comparison of low-dose CT with adaptive statistical iterative reconstruction and routine-dose CT with filtered back projection in 53 patients. AJR Am J Roentgenol 195:713–719
16. Singh S, Kalra MK, Gilman MD et al (2011) Adaptive statistical iterative reconstruction technique for radiation dose reduction in chest CT: A pilot study. Radiology 259:565–573
17. Singh S, Kalra MK, Hsieh J et al (2010) Abdominal CT: Comparison of adaptive statistical iterative and filtered back projection reconstruction techniques. Radiology 257:373–383
18. Cornfeld D, Israel G, Detroy E, Bokhari J, Mojibian H (2011) Impact of adaptive statistical iterative reconstruction (ASIR) on radiation dose and image quality in aortic dissection studies: A qualitative and quantitative analysis. AJR Am J Roentgenol 196: W336–W340
19. Thibault JB, Sauer KD, Bouman CA, Hsieh J (2007) A three-dimensional statistical approach to improved image quality for multislice helical CT. Med Phys 34:4526–4544
20. Yu Z, Thibault JB, Bouman CA, Sauer KD, Hsieh J (2011) Fast model-based X-ray CT reconstruction using spatially nonhomogeneous ICD optimization. IEEE Trans Image Process 20:161–175
21. Strub WM, Weiss KL, Sun D (2007) Hybrid reconstruction kernel: Optimized chest CT. AJR Am J Roentgenol 189: W115–W116
22. Weiss KL, Cornelius RS, Greeley AL et al (2011) Hybrid convolution kernel: Optimized CT of the head, neck, and spine. AJR Am J Roentgenol 196:403–406
23. Prakash P, Kalra MK, Ackman JB et al (2010) Diffuse lung disease: CT of the chest with adaptive statistical iterative reconstruction technique. Radiology 256:261–269
24. National Lung Screening Trial Research Team, Aberle DR, Berg CD et al (2011) The National Lung Screening Trial: overview and study design. Radiology 258:243–253
25. Shrimpton PC, Hillier MC, Lewis MA, Dunn M (2006) National survey of doses from CT in the UK: 2003. Br J Radiol 79:968–980
26. EUR 16262. European guidelines on quality criteria for computed tomography. www.drs.dk/guidelines/ct/quality/. Accessed 10 February 2012

Jpn J Radiol (2012) 30:34–39
DOI 10.1007/s11604-011-0004-0

ORIGINAL ARTICLE

Precision of the measurement of CT numbers: comparison of dual-energy CT spectral imaging with fast kVp switching and conventional CT with phantoms

Izuru Matsuda · Masaaki Akahane · Jiro Sato · Masaki Katsura · Shigeru Kiryu · Naoki Yoshioka · Akira Kunimatsu · Kenji Ino · Kuni Ohtomo

Received: 27 May 2011 / Accepted: 21 July 2011 / Published online: 2 December 2011

Abstract
Purpose To compare dual-energy computed tomography (CT) spectral imaging and conventional CT imaging in terms of precision of the measurement of CT numbers in phantoms.
Materials and methods A circular phantom (CP) and an elliptical phantom (EP) were used. Capsules filled with iodine contrast media solutions at various concentration levels were placed in the phantoms. Conventional CT was performed at a tube voltage of 120 kVp. Simulated monochromatic images at 65 keV were obtained by dual-energy CT spectral imaging. The CT number of each iodine capsule was measured. A linear regression model was used to evaluate linearity, while analysis of covariance was used to investigate the degree of variability according to phantom shape for each imaging method.
Results With conventional imaging, the slopes of the regression lines for CT numbers measured at the EP center and EP periphery were significantly lower than those measured for CP ($P < 0.0001$ for both EP center vs. CP and for EP periphery vs. CP). No significant difference in slope was found among phantom shapes in dual-energy spectral CT imaging.
Conclusion Computed tomography numbers varied considerably depending on the phantom shape in conventional CT, whereas dual-energy CT provided consistent CT numbers regardless of the phantom shape.

Keywords Dual-energy CT · CT number · Precision · Phantom · Monochromatic imaging

I. Matsuda (✉) · M. Akahane · J. Sato · M. Katsura · A. Kunimatsu · K. Ohtomo
Department of Radiology, Graduate School of Medicine, The University of Tokyo, 7-3-1 Hongo, Bunkyo-ku, Tokyo 113-8655, Japan
e-mail: imatsuda-tky@umin.ac.jp

S. Kiryu
Department of Radiology, Institute of Medical Science, The University of Tokyo, 4-6-1 Shirokanedai, Minato-ku, Tokyo 108-8639, Japan

N. Yoshioka
Department of Integrated Imaging Informatics, The University of Tokyo Hospital, 7-3-1 Hongo, Bunkyo-ku, Tokyo 113-8655, Japan

K. Ino
Department of Clinical Radiology, The University of Tokyo Hospital, 7-3-1 Hongo, Bunkyo-ku, Tokyo 113-8655, Japan

Introduction

Computed tomography (CT) number is a calculated value and an estimate of the X-ray attenuation coefficient of a voxel, generally expressed in Hounsfield units (HU), where the CT number of air is −1000 HU and that of water is 0 HU. Despite its seemingly physical definition, values are reported to be variable, being dependent on factors such as the model of CT scanner, tube voltage, reconstruction algorithm, and distribution of the examined object [1–4]. A clinical example of the poor reproducibility of CT number has been reported as pseudoenhancement, such as increased attenuation of small simple renal cysts on contrast-enhanced CT scans [5–13].

Dual-energy CT methods are one of the most promising recent technological advances in CT. CT data acquisition is generally performed using a particular X-ray tube potential. By using two different X-ray spectra, dual-energy CT can distinguish pixels with the same CT number but that

consist of different materials, e.g., calcium, iodine, or uric acid [14–16]. In measuring the X-ray attenuation of an object using two different spectra, it is possible to resolve attenuation measurements in the density of two arbitrarily chosen materials. This mathematical process is termed 'material decomposition' [17]. Using this method, monochromatic images are synthesized from the material density images. The monochromatic image is the virtual image that would be obtained if the X-ray source produced only X-ray photons at a single energy. In general, the monochromatic image is similar to a conventional CT image, but has fewer artifacts, particularly beam-hardening artifacts [18].

One of the causes of the poor reproducibility of CT numbers is thought to be nonlinear errors due to scatter in attenuation measurement, which is difficult to correct adequately [19]. Also, it was reported that the material decomposition process in dual-energy CT imaging methods had a compensating effect for scatter [20]. The purpose of the present study is to compare dual-energy CT spectral imaging and conventional CT imaging in terms of the precision of measurements of CT numbers with phantoms.

Materials and methods

Phantoms

We used a 15-cm-diameter circular phantom (CP) and an elliptical phantom (EP), 22 cm in the anterior-posterior direction and 33 cm in the lateral direction, to evaluate the effect of the surrounding density distribution on CT number (Fig. 1). The CP was made of 15-cm-thick tough-water equivalent phantom (Kyoto Kagaku, Kyoto, Japan). Optimal CT number measurement with less error was represented by measurement in the CP. Five cylindrical holes of 1 cm diameter were placed circularly on the CP.

The EP (Multislice CT phantom MHT type; Kyoto Kagaku, Kyoto, Japan) was made of polyurethane with cylindrical holes located in the center and at the 15 cm periphery from the center along the long axis. The EP was used as an imitation of the human body with similar shape, size, and density, and was expected to cause scatter and CT number measurement error. CT scans were acquired after placement, into the holes of the phantoms, of micro test tubes filled with a dilution series of iodine contrast media. Iodine contrast media of 300 mg I/ml (iohexol, Omnipaque 300 Syringe; Daiichi Sankyo, Tokyo, Japan) was diluted by 5% to make a dilution equivalent to 15 mg I/ml iodine solution. Then twofold serial dilution was performed to make dilutions equivalent to 1.875, 3.75, and 7.5 mg I/ml iodine solution. Pure water was used as 0 mg I/ml solution.

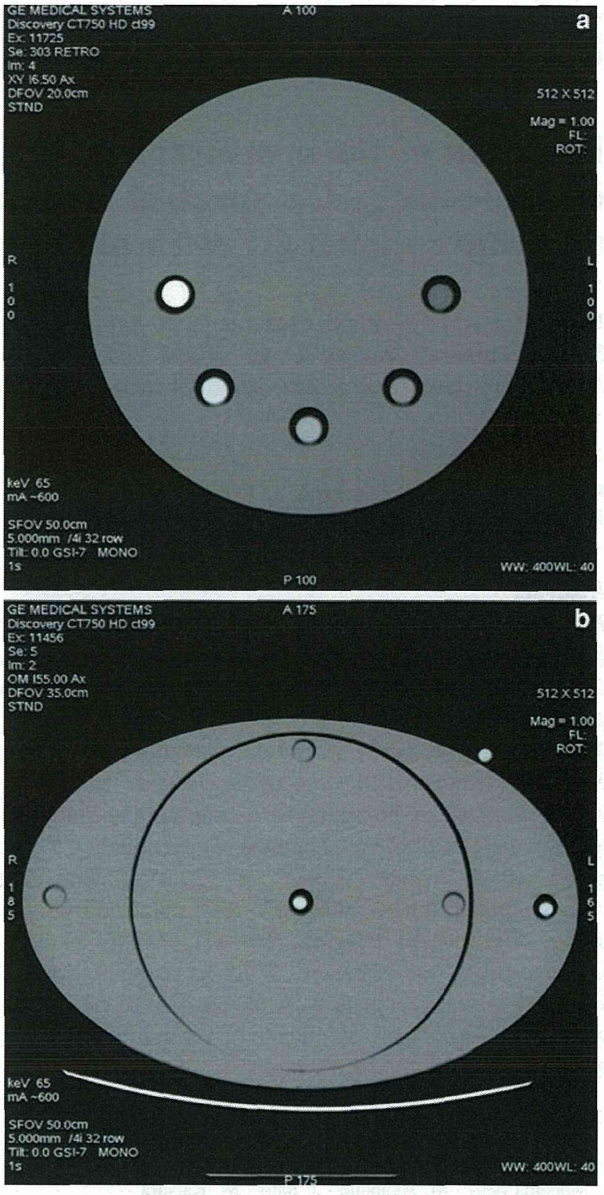

Fig. 1 **a** Simulated monochromatic CT image at 65 keV shows a sectional view of the circular phantom. The micro test tubes are filled with iodine contrast medium solutions at various concentrations. **b** Simulated monochromatic CT image at 65 keV shows a sectional view of the elliptical phantom. The *holes at the center* and at the 15 cm periphery along the *long axis* were used to evaluate the CT number of each solution of the iodine contrast media

CT imaging and measurement

Scans were acquired with a 64-slice CT system (Discovery CT 750HD; GE Healthcare). All examinations were performed in axial scanning mode with a large body filter. Conventional CT images were acquired with a tube potential of 120 kVp and tube current of 410 mA. Simulated monochromatic images at 65 keV were obtained by dual-energy CT spectral imaging

with fast kVp switching between 80 and 140 kVp, with a tube current of 600 mA. The tube current was set to adjust the volume computed tomography dose index ($CTDI_{vol}$) to a level similar to that in conventional CT. We chose a value of 65 keV for the simulated monochromatic images because CT numbers of water measured at 65 keV are similar to those measured in conventional imaging at tube potential of 120 kVp. Scanning was performed with the phantoms placed at the center of the scan field. The following parameters were used in both imaging techniques: detector coverage, 20 mm; slice thickness, 5.0 mm; rotation time, 1.0 s; scanned field-of-view, 50 cm. All images were reconstructed using STANDARD kernel with the target micro test tubes located at the center of the reconstructed image and a 20-cm field of view. Appropriate slices were selected to avoid partial volume effects at the ends of the tubes, and mean CT numbers were measured one time in HU using a circular region of interest (ROI) that was carefully placed at the center of the cross-sectional image of each tube. Area of the ROI was 20 mm^2, and the ROI was replicated with copy function on a workstation to measure all the tubes. $CTDI_{vol}$ values were recorded during CT scanning to evaluate radiation exposure.

Statistical analysis

A linear regression model was used to evaluate linearity. Variability of the CT numbers for each imaging method was investigated in terms of phantom shape using analysis of covariance with Bonferroni multiple-comparison correction. All statistical computations were performed using JMP software (version 8.0.2, SAS Institute Japan, Tokyo, Japan).

Results

Computed tomography numbers in HU corresponding to iodine concentration at 0, 1.875, 3.75, 7.5 and 15 mg I/ml were 2.31, 49.35, 99.84, 197.21 and 406.79, respectively, when using conventional image and the CP hole. Those for conventional image and the EP central and peripheral hole, and for simulated monochromatic image and the CP, EP central and peripheral hole were −2.67, 33.93, 77.10, 157.50 and 328.66; 1.11, 38.48, 84.97, 167.74 and 345.99; 2.22, 50.92, 103.49, 206.66 and 431.85; −2.08, 44.77, 95.98, 195.66 and 405.83; and 2.09, 46.49, 95.76, 198.35 and 413.55, respectively. Slopes of regression lines of the measured CT numbers for conventional image and the CP, EP central and peripheral hole, and simulated monochromatic image and the CP, EP central and peripheral hole were 27.01, 22.18, 23.10, 28.72, 27.27 and 27.61, respectively. There was a uniformly high correlation of CT number with iodine concentration, regardless of the combination of phantom and CT imaging method used (Table 1; Fig. 2). The coefficient of determination was above 0.999 under all experimental conditions.

In the conventional CT method, significant difference was found regarding the slope of the linear relation between CT number and concentration measured in the EP compared with those in the CP, although linearity was good for both phantoms, whereas no significant difference was found in measured slope for the simulated monochromatic images (Table 2). The mean CT numbers are presented in Table 1. The CT number for water density was approximately 0 HU (mean ± standard deviation, 0.50 ± 2.27) under all conditions.

$CTDI_{vol}$ values were 34.87 mGy for conventional CT and 36.18 mGy for dual-energy CT spectral imaging with fast kVp switching.

Discussion

Although both conventional and simulated monochromatic imaging achieved very high linearity of CT numbers in

Table 1 Measured CT numbers and regression parameters

Iodine concentration (mg I/ml)	Conventional-CP	Conventional-EP central	Conventional-EP peripheral	Simulated monochromatic-CP	Simulated monochromatic-EP central	Simulated monochromatic-EP peripheral
0	2.31	−2.67	1.11	2.22	−2.08	2.09
1.875	49.35	33.93	38.48	50.92	44.77	46.49
3.75	99.84	77.10	84.97	103.49	95.98	95.76
7.5	197.21	157.50	167.74	206.66	195.66	198.35
15	406.79	328.66	345.99	431.85	405.83	413.55
Regression parameters						
Slope	27.01	22.18	23.10	28.72	27.27	27.61
Y intercept	−0.83	−5.88	−2.27	−2.52	−5.38	−4.08
Coefficients of determination	0.9996	0.9996	0.9996	0.9993	0.9997	0.9992

CP circular phantom, *EP* elliptical phantom

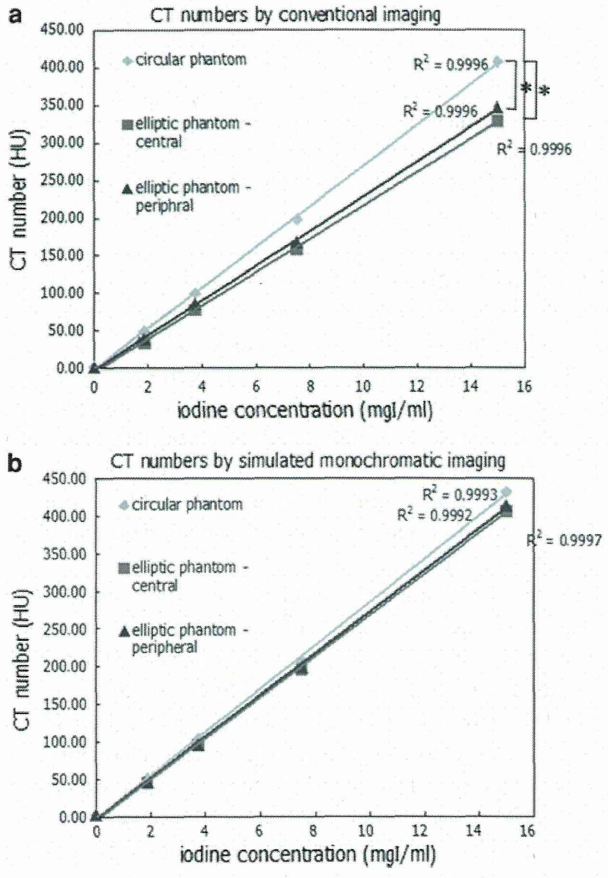

Fig. 2 **a** *Plots* of the CT numbers acquired with conventional CT imaging and their regression lines. All coefficients of determination (R^2) were above 0.999. The slopes of the regression lines calculated using the data from the center and the periphery of the elliptical phantom show a statistically significant difference compared with those of the circular phantom. **b** *Plots* of the CT numbers acquired with simulated monochromatic imaging using dual-energy CT and their regression lines. All coefficients of determination (R^2) were above 0.999. There was no statistically significant difference in slope among the three regression lines

terms of iodine concentration, consistent slopes were not attained in the conventional imaging method. Conventional imaging did not yield consistent CT numbers for the same iodine solution in differently shaped phantoms. In contrast, simulated monochromatic imaging produced almost the same CT numbers regardless of phantom shape. These results suggest that simulated monochromatic imaging using dual-energy spectral CT potentially enables better reproducibility of CT numbers, at least for iodine contrast media solutions, without influence from the surrounding environment.

It is possible that artifacts such as streaks could have affected the present results; however, none of the images acquired in our experiments demonstrated obvious undesirable artifacts. The very high linearity observed for all imaging methods and phantoms supports the assumption

Table 2 Comparisons of the slopes of CT numbers

	P value
Conventional imaging	
Circular versus elliptical central	<0.0001*
Circular versus elliptical peripheral	<0.0001*
Elliptical central versus elliptical peripheral	0.0482
Simulated monochromatic imaging	
Circular versus elliptical central	0.0281
Circular versus elliptical peripheral	0.1267
Elliptical central versus elliptical peripheral	0.5404

P values were calculated using analysis of covariance. $P < 0.0083$ was considered statistically significant with Bonferroni multiple-comparison correction

* Statistically significant

that focal artifacts do not cause slope inconsistency in conventional imaging; rather, a more diffuse variation of CT numbers exists that can be eliminated by using dual-energy CT imaging. In previously published papers, beam hardening has been frequently mentioned as a cause of pseudoenhancement [5–13]. When lower energy photons of the beam are preferentially attenuated by higher density material than water, and images are reconstructed with an algorithm that compensates the excessive attenuation, beam hardening occurs. Accuracy in CT number in our experiments using simulated monochromatic images was achieved at least partly because the beam-hardening effect was corrected with dual-energy measurements [17]. Additionally, in our experiment, CT number inconsistency was found in the measurements with EP that had similar size and density to the patient's body. Body-sized objects cause scatter and give rise to CT number measurement error, as Joseph et al. [19] demonstrated. Simulated monochromatic images might be accurate in CT number measurement because the error induced by scatter was compensated in the process of material decomposition, as Vetter et al. [20] indicated.

Clinically, increased attenuation of small simple renal cysts on contrast-enhanced CT is reported as 'pseudoenhancement;' however, enhancement of a renal mass on contrast-enhanced CT is an essential criterion for distinguishing between tumors and benign cysts [5–13]. The present results show the effect of the shape of surrounding tissue on the CT number of the lesion of interest. Essentially, variability in the shape of the surrounding tissue means that the distribution of density also varies. The density distribution in a contrast-enhanced CT image is substantially different from that in a plain CT image; one possible cause of pseudoenhancement may be this change in density distribution. The present results indicate that it may be possible to apply dual-energy CT to eliminate undesirable effects of the surrounding environment that

affect the CT number of the lesion of interest, to achieve accurate CT number acquisition. Furthermore, simulated monochromatic images created with dual-energy CT may enable more accurate diagnoses dependent on CT number measurement such as distinction between adrenal adenoma and other tumors [21–24] because the accuracy of CT number measurement without the influence of body shape means robustness against individual differences.

A potential disadvantage of dual-energy spectral CT is increased radiation exposure. In our experiment, however, the $CTDI_{vol}$ values for dual-energy CT spectral imaging were almost equivalent to conventional CT imaging. Although we did not assess image quality closely, standard deviation of background noise was below 10 HU in both the conventional and simulated monochromatic images. Both image sets seemed to show almost the same image quality subjectively. Simulated monochromatic images were capable of substituting for conventional CT images in this regard.

The present study has some limitations. We chose 65 keV as a parameter for simulated monochromatic imaging because these images have CT numbers similar to those of images acquired at 120 kVp in conventional imaging. However, we did not investigate optimal keV values for CT number reproducibility. In addition, this study was conducted as a phantom study, and clinical feasibility was not investigated.

The present results in a phantom study demonstrated that CT number consistency was better achieved by dual-energy spectral CT imaging than by conventional CT imaging. This result has some possible practical applications in clinical CT. Using the dual-energy spectral CT imaging method, precise measurement of CT number could be obtained, thereby enabling more accurate comparison of the densities of lesions of interest. In conclusion, the measured CT attenuation numbers of water solutions of iodine contrast media varied depending on phantom shape, and dual-energy CT spectral imaging using simulated monochromatic images achieved better CT number consistency than that obtained using conventional CT imaging.

Acknowledgments We gratefully acknowledge Kosuke Sasaki, M.S., and Koji Segawa, R.T., for their technical support and assistance in data acquisition.

References

1. Levi C, Gray J, McCullough E, Hattery R. The unreliability of CT numbers as absolute values. Am J Roentgenol. 1982;139:443–7.
2. Zerhouni EA, Spivey JF, Morgan RH, Leo FP, Stitik FPa, Siegelman SS. Factors influencing quantitative CT measurements of solitary pulmonary nodules. J Comput Assist Tomogr. 1982;6:1075–87.
3. McCullough E, Morin R. CT-number variability in thoracic geometry. Am J Roentgenol. 1983;141:135–40.
4. Birnbaum BA, Hindman N, Lee J, Babb JS. Multi-detector row CT Attenuation measurements: assessment of intra- and interscanner variability with an anthropomorphic body CT phantom. Radiology. 2007;242:109–19.
5. Maki DD, Birnbaum BA, Chakraborty DP, Jacobs JE, Carvalho BM, Herman GT. Renal cyst pseudoenhancement: beam-hardening effects on CT numbers. Radiology. 1999;213:468–72.
6. Coulam CH, Sheafor DH, Leder RA, Paulson EK, DeLong DM, Nelson RC. Evaluation of pseudoenhancement of renal cysts during contrast-enhanced CT. Am J Roentgenol. 2000;174:493–8.
7. Bae KT, Heiken JP, Siegel CL, Bennett HF. Renal cysts: is attenuation artifactually increased on contrast-enhanced CT images? Radiology. 2000;216:792–6.
8. Birnbaum BA, Maki DD, Chakraborty DP, Jacobs JE, Babb JS. Renal cyst pseudoenhancement: evaluation with an anthropomorphic body CT phantom. Radiology. 2002;225:83–90.
9. Abdulla C, Kalra MK, Saini S, Maher MM, Ahmad A, Halpern E, et al. Pseudoenhancement of simulated renal cysts in a phantom using Different multidetector CT scanners. Am J Roentgenol. 2002;179:1473–6.
10. Heneghan JP, Spielmann AL, Sheafor DH, Kliewer MA, DeLong DM, Nelson RC. Pseudoenhancement of simple renal cysts: a comparison of single and multidetector helical CT. J Comput Assist Tomogr. 2002;26:90–4.
11. Israel GM, Bosniak MA. Pitfalls in renal mass evaluation and how to avoid them. Radiographics. 2008;28:1325–38.
12. Birnbaum BA, Hindman N, Lee J, Babb JS. Renal cyst pseudoenhancement: influence of multidetector CT reconstruction algorithm and scanner type in phantom model. Radiology. 2007;244:767–75.
13. Wang ZJ, Coakley FV, Fu Y, Joe BN, Prevrhal S, Landeras LA, et al. Renal cyst pseudoenhancement at multidetector CT: what are the effects of number of detectors and peak tube voltage? Radiology. 2008;248:910–6.
14. Graser A, Johnson TRC, Bader M, Staehler M, Haseke N, Nikolaou K, et al. Dual energy CT characterization of urinary calculi: initial in vitro and clinical experience. Invest Radiol. 2008;43:112–9.
15. Boll DT, Patil NA, Paulson EK, Merkle EM, Simmons WN, Pierre SA, et al. Renal stone assessment with dual-energy multidetector CT and advanced postprocessing techniques: improved characterization of renal stone composition—pilot study. Radiology. 2009;250:813–20.
16. Thomas C, Patschan O, Ketelsen D, Tsiflikas I, Reimann A, Brodoefel H, et al. Dual-energy CT for the characterization of urinary calculi: in vitro and in vivo evaluation of a low-dose scanning protocol. Eur Radiol. 2009;19:1553–9.
17. Alvarez RE, Macovski A. Energy-selective reconstruction in X-ray computerized tomography. Phys Med Biol. 1976;21:733–44.
18. Wu X, Langan DA, Xu D, Benson TM, Pack JD, Schmitz AM, et al. Monochromatic CT image representation via fast switching dual kVp. In: Proceedings of the SPIE, vol. 7258; 2009. p. 725845.
19. Joseph PM, Spital RD. The effects of scatter in X-ray computed tomography. Med Phys. 1982;9:464–72.
20. Vetter JR, Holden JE. Correction for scattered radiation and other background signals in dual-energy computed tomography material thickness measurements. Med Phys. 1988;15:726–31.
21. van Erkel AR, van Gils AP, Lequin M, Kruitwagen C, Bloem JL, Falke TH. CT and MR distinction of adenomas and non-adenomas of the adrenal gland. J Comput Assist Tomogr. 1994;18:432–8.

22. McNicholas MM, Lee MJ, Mayo-Smith WW, Hahn PF, Boland GW, Mueller PR. An imaging algorithm for the differential diagnosis of adrenal adenomas and metastases. Am J Roentgenol. 1995;165:1453–9.
23. Miyake H, Takaki H, Matsumoto S, Yoshida S, Maeda T, Mori H. Adrenal nonhyperfunctioning adenoma and nonadenoma: CT attenuation value as discriminative index. Abdom Imaging. 1995;20:559–62.
24. Korobkin M, Brodeur FJ, Yutzy GG, Francis IR, Quint LE, Dunnick NR, et al. Differentiation of adrenal adenomas from nonadenomas using CT attenuation values. Am J Roentgenol. 1996;166:531–6.

Jpn J Radiol (2012) 30:146–153
DOI 10.1007/s11604-011-0026-7

ORIGINAL ARTICLE

Effect of radiation dose and adaptive statistical iterative reconstruction on image quality of pulmonary computed tomography

Jiro Sato · Masaaki Akahane · Sachiko Inano · Mariko Terasaki · Hiroyuki Akai · Masaki Katsura · Izuru Matsuda · Akira Kunimatsu · Kuni Ohtomo

Received: 3 July 2011 / Accepted: 1 October 2011 / Published online: 17 December 2011

Abstract
Purpose The purpose of this study was to assess the effects of dose and adaptive statistical iterative reconstruction (ASIR) on image quality of pulmonary computed tomography (CT).
Materials and methods Inflated and fixed porcine lungs were scanned with a 64-slice CT system at 10, 20, 40 and 400 mAs. Using automatic exposure control, 40 mAs was chosen as standard dose. Scan data were reconstructed with filtered back projection (FBP) and ASIR. Image pairs were obtained by factorial combination of images at a selected level. Using a 21-point scale, three experienced radiologists independently rated differences in quality between adjacently displayed paired images for image noise, image sharpness and conspicuity of tiny nodules. A subjective quality score (SQS) for each image was computed based on Anderson's functional measurement theory. The standard deviation was recorded as a quantitative noise measurement.
Results At all doses examined, SQSs improved with ASIR for all evaluation items. No significant differences were noted between the SQSs for 40%-ASIR images obtained at 20 mAs and those for FBP images at 40 mAs.
Conclusion Compared to the FBP algorithm, ASIR for lung CT can enable an approximately 50% dose reduction from the standard dose while preserving visualization of small structures.

Keywords Computed tomography · Iterative reconstruction · Dose reduction · Image quality

J. Sato (✉) · M. Akahane · S. Inano · M. Terasaki · H. Akai · M. Katsura · I. Matsuda · A. Kunimatsu · K. Ohtomo
Department of Radiology, Graduate School of Medicine, The University of Tokyo, 7-3-1 Hongo, Bunkyo-ku, Tokyo 113-8655, Japan
e-mail: jsato-tky@umin.ac.jp

M. Akahane
e-mail: akahane-tky@umin.ac.jp

S. Inano
e-mail: dzsachi@hotmail.com

M. Terasaki
e-mail: hasimari-1101@hotmail.co.jp

H. Akai
e-mail: commonhiro@hotmail.com

M. Katsura
e-mail: mskktsr@gmail.com

I. Matsuda
e-mail: imatsudajp@yahoo.co.jp

A. Kunimatsu
e-mail: akrk-tky@umin.ac.jp

K. Ohtomo
e-mail: kotomo-tky@umin.ac.jp

Introduction

Worldwide, the number of CT examinations has escalated from one to three procedures per 1000 people during 1977–1980 to about 35 procedures per 1000 people during 1997–2007 [1]. CT accounts for more than 40% of the collective effective dose of medical radiation worldwide [1], and 0.6–3.2% of the cumulative risk of cancer until the age of 75 could be attributable to diagnostic exposure in developed countries [2]. Thus, public concerns about medical radiation exposure and dose reduction have been growing. Reducing the dose, however, results in an increase in image noise that degrades image quality with the standard filtered back projection (FBP) reconstruction. Some image filters can reduce noise, but use of them tends

to be restricted particularly in chest CT owing to concomitant degradation of spatial resolution, since image sharpness is critical for interpretation of the lung [3].

The iterative reconstruction technique, which has recently become available on commercial CT scanners, enables noise reduction with essentially no trade-off in spatial resolution [4]. Previous studies for chest CT showed that iterative reconstruction helped reduce the radiation dose and improve image quality by reducing noise compared with the conventional FBP technique [5–8]. Iterative reconstruction, however, is not free from unfavorable effects. Use of it alters the texture of image noise and can yield a unusually homogenous image, which may not be immediately appealing to most radiologists usually accustomed to the FBP image [9]. It is also known that an excessive degree of iterative reconstruction may obscure fine and subtle findings [7].

In this study, we focused on subjective assessment of image quality using a method based on Anderson's functional measurement theory. The theory was originally developed for description of non-observable psychological processes and has been applied efficiently to image quality assessment [10–12]. With this method, the subjective image quality can be represented as a score on an interval scale, facilitating comparison of quality of images obtained with different parameters.

The aims of this study were to assess the effect of iterative reconstruction on the quality of lung CT images in relation to radiation dose and to investigate attainable degree of dose reduction compared with FBP.

Materials and methods

Image acquisition

One pair of porcine lungs inflated and fixed with Heitzman's method [13] placed in an oval polymethylmethacrylate phantom with a long axis of 33.3 cm and a short axis of 23.1 cm was scanned with a 64-slice CT system (Discovery CT 750HD; GE Healthcare, Milwaukee, WI). Since the lungs used are small (about 11 cm in the longest diameter) and have no other extra-thoracic soft tissue except for the thoracic vertebra and rib cage, a smaller radiation dose was likely to be sufficient compared with standard dose for human lungs. Therefore, we assumed a standard dose for the porcine lungs using automatic exposure control of the scanner (AutomA; GE Healthcare) to keep the noise level similar to routine clinical lung CT. Using AutomA, a tube current time product of 40 mAs was chosen as standard, with a noise index of 11 for a 5-mm-thick image and a standard reconstruction kernel. A half dose and a quarter dose of the standard (i.e., 20 and 10 mAs) were also used for reduced-dose mode, and a 400-mAs dose was used to create high-quality images. Helical scans were performed with scanning parameters including a tube voltage of 120 kVp, a detector configuration of 64 × 0.625 mm and a beam pitch of 0.984:1. Image data were reconstructed with an FBP algorithm with a standard kernel into 5-mm-thick axial images with 512 × 512 pixels and a 350-mm field of view. The data obtained at 10, 20 and 40 mAs were also reconstructed with ASIR, an implementation of iterative reconstruction techniques (Table 1). In reconstruction with ASIR, the original FBP and the fully converged ASIR (100%-ASIR) images are blended to give the final ASIR image. Although increasing the ratio of the full ASIR data to the FBP data results in reduction of image noise, it also changes the texture of noise and may cause loss of diagnostic information. Because of the paucity of available data about appropriate blending ratio of ASIR for chest CT at the time of the experiment, we chose blending ratios of 20 and 40% according to the result of a previous study [9].

Using picture archiving and communication system equipment (Centricity; GE Healthcare, Milwaukee, WI) with a DICOM-compliant 21-inch 2-megapixel liquid crystal display (LCD) monitor (Radiforce R22; Eizo Nanao, Ishikawa, Japan), one of the authors with 11 years' experience in reading lung CT images selected a slice without major artifacts from the image set obtained at 400 mAs. This image was saved into a TIFF format file with a fixed lung window setting (window width and level were 600 and −900, respectively). The window was determined so that CT images of the fixed porcine lungs resembled typical human lung CT images in terms of subjective image noise and visually reproduction of lung structures. Images at the same slice level with different doses or reconstruction methods were saved in a similar

Table 1 Doses and algorithms used for image acquisition and reconstruction

Image	Dose (mAs)	Reconstruction
A_0	10	FBP
A_{20}	10	20%-ASIR
A_{40}	10	40%-ASIR
B_0	20	FBP
B_{20}	20	20%-ASIR
B_{40}	20	40%-ASIR
C_0	40	FBP
C_{20}	40	20%-ASIR
C_{40}	40	40%-ASIR
D_0	400	FBP

FBP filtered back projection, *ASIR* adaptive statistical iterative reconstruction

manner. Images were then cropped to 256 × 256 pixels by trimming a peripheral portion out of the thoracic cage with ImageJ software (ImageJ, version 1.42; National Institutes of Health, Bethesda, MD). The ten resulting images were evaluated in the current study (Fig. 1).

Qualitative analysis

One trained and two board-certified radiologists with 4, 7 and 7 years' experience in reading chest CT images independently evaluated the quality of each image in the following three areas: noise of lung parenchyma, image sharpness and conspicuity of tiny nodules. For evaluating image sharpness, readers were asked to evaluate the sharpness of the walls of the bronchovascular structures and the extent to which the peripheries of the structures were visible. Nodules were about 1 mm in diameter and predominantly seen in peripheral areas of the lungs, indicating probable calcified granulomas. Experiments were performed based on Anderson's functional measurement theory [10, 11, 14]. It was originally developed in the area of psychology and has been applied efficiently to image quality assessment [10–12]. Experiments using the theory involve three steps: showing images as a pair, rating the perceived difference in image quality and calculating subjective quality scores (SQSs). To display images and

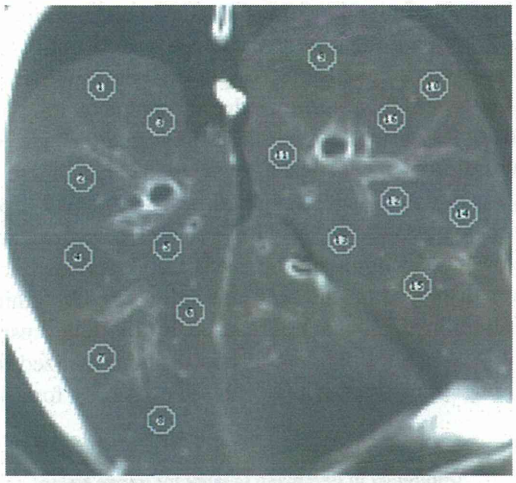

Fig. 2 16 circular regions of interest (ROIs) with a size of 24.3 mm^2 are placed on lung parenchyma, avoiding apparent structures and major artifacts. The 16 measurements for each image were averaged. To measure at the same positions, ROIs were copied between images

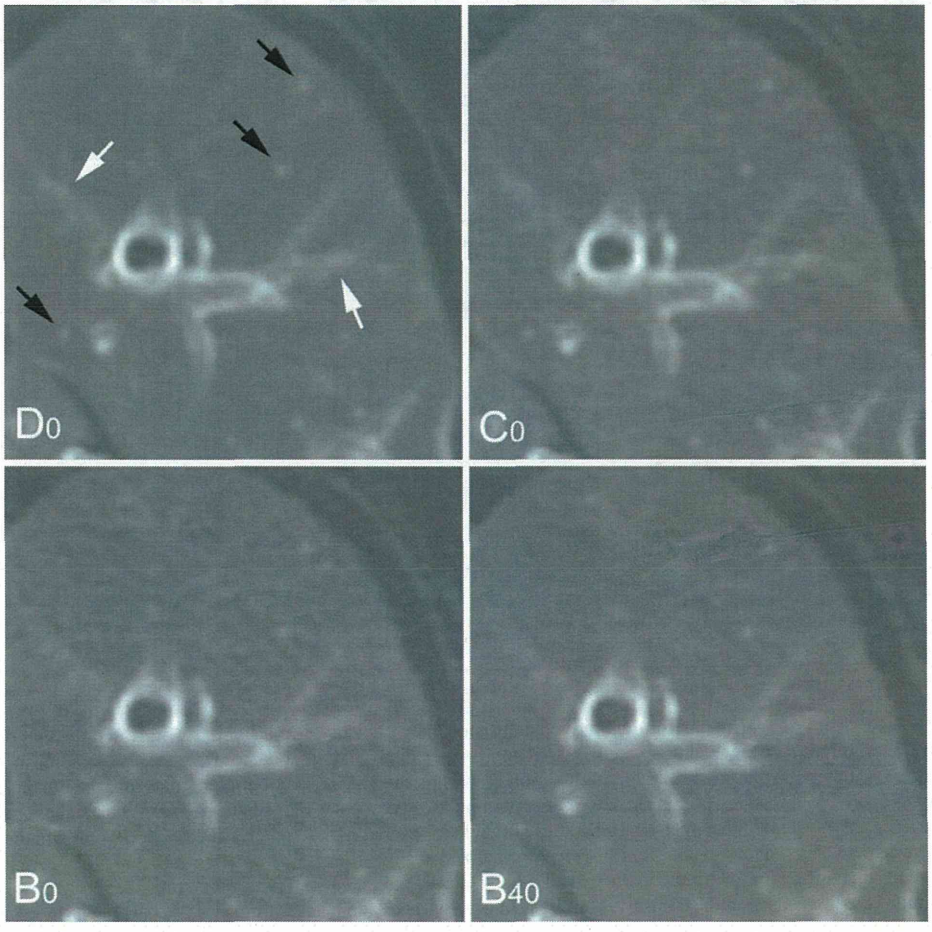

Fig. 1 *Upper left* image D_0, *upper right* image C_0, *lower left* image B_0, *lower right* image B_{40}. *Black arrows* in image D_0 indicate tiny nodules and *white arrows* bronchovascular structures. Compared with image C_0, image B_0, which was obtained at a half dose, appears noisy, and bronchovascular structures and nodules on image B_0 are blurred. The subjective quality scores (SQSs) for image B_0 were significantly lower than those for image C_0 for noise (−0.41 vs. 0.47, $P < 0.001$) and for sharpness (−0.18 vs. 0.64, $P = 0.015$). From comparison between image B_0 and image B_{40}, image quality apparently improved with 40% ASIR. The SQSs for image B_{40} were comparable to those for image C_0 on noise (0.43 vs. 0.47, $P > 0.999$). Although no statistically significant results were observed, sharpness was worse on B_{40} than on C_0 (0.43 vs. 0.64, $P = 0.985$), and conspicuity of nodules was better on B_{40} than on C_0 (0.70 vs. 0.37, $P = 0.551$)

record the reader's rating, an in-house program written in JAVA language running on the PACS system was used. One hundred image pairs, generated by a factorial combination of the ten prepared images, were presented on the LCD monitor in random order. Readers rated differences in quality between adjacently displayed paired images from −10 to 10, using a slider displayed below the images, without time limits or knowledge of parameters for image acquisition. The sign of the scores indicated the side of the preferred image. For each evaluation area, presenting image pairs twice and averaging the scores of two sessions yielded a 10 × 10 matrix with elements of scores, where the row and column of the matrix corresponded to the images displayed on the right and left sides. To minimize the interindividual variation caused by the range used in rating, elements of the data matrix were normalized using the z score transformation [10, 11]. The z score z for a score s is given by $z = (s - \mu)/\sigma$, where μ and σ are the mean and standard deviation of scores. Before the calculation based on the Anderson's functional measurement theory, it is required to observe parallelism for data within the different rows and columns of the matrix graphically or to calculate the interaction between rows and columns by means of two-way analysis of variance method (ANOVA) [10, 11]. Then the SQS for image i, SQS_i, can be calculated from the data matrix as follows, according to the theory,

$$SQS_i = \frac{\bar{r}_{i\bullet} - \bar{r}_{\bullet i}}{2}.$$

Here $\bar{r}_{i\bullet}$ represents the marginal mean for row i of the matrix, and $\bar{r}_{\bullet i}$ represents the marginal mean for column i of the matrix. Before an actual test session, readers practiced for several minutes with an image set consisting of images at the 1 cm caudal level, in order to become

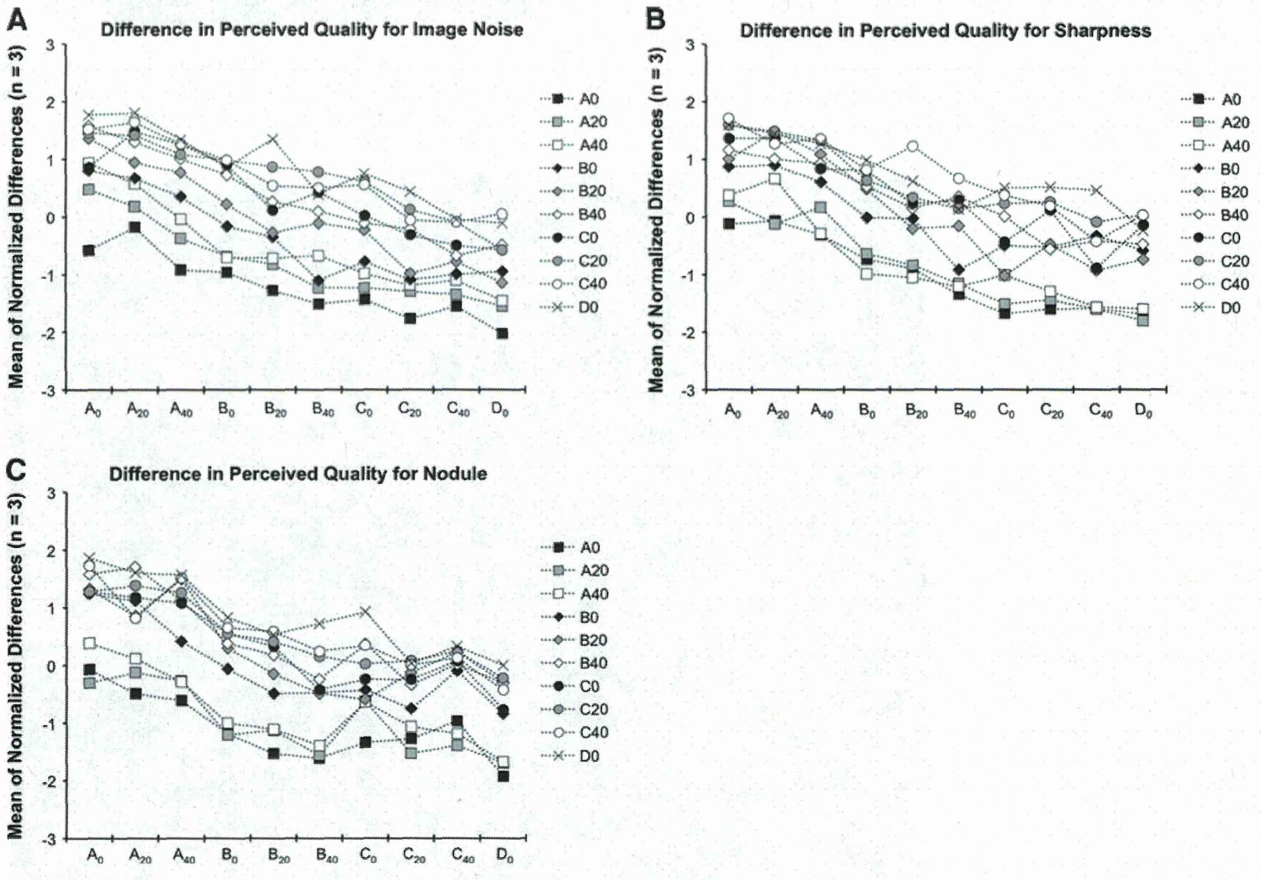

Fig. 3 Result of experiments for qualitative analysis of image noise, averaged for all readers. Each curve corresponds to images displayed on the right side of the monitor, and the label on the x axis indicates images on the left side. Points on curves correspond to perceived difference in quality between paired images. Before averaging between readers, individual scores were normalized using the z score transformation. Note the approximate parallelism of the data. Similar parallelisms were also observed on both image sharpness and conspicuity of tiny nodules. To observe parallelism of data graphically or, more preferably, to confirm no interaction between the rows and columns of data matrix by means of two-way analysis of variance method (ANOVA) is necessary for calculation for the subjective quality score for each image based on Anderson's functional measurement theory. Result of two-way ANOVA showed no significant interactions between rows and columns of the data ($P = 0.248$ for noise, $P = 0.717$ for sharpness and $P = 0.867$ for nodules)

familiar with the method of evaluation and the range of image quality.

To minimize the increased risk of type I errors due to multiple testing, SQSs were analyzed by Tukey's honestly significant differences test using a statistical suite (R, version 2.9.2; http://www.R-project.org, R Foundation for Statistical Computing, Vienna, Austria).

Quantitative analysis

An experienced radiologist measured the standard deviation of attenuation values (image SD) as quantitative noise data with ImageJ by placing 16 circular regions of interest (ROIs) with a size of 24.3 mm^2 on lung parenchyma, avoiding apparent structures and major artifacts (Fig. 2). The 16 measurements for each image were averaged. To measure at the same positions, ROIs were copied between images. Pearson's correlation coefficients between image SDs and SQSs were calculated.

Results

Figure 3 shows approximate parallelism of data in the rating of experiments for image noise. After no significant row-column interaction was confirmed using two-way ANOVA tests ($P = 0.248$ for noise, $P = 0.717$ for sharpness and $P = 0.867$ for nodules), SQSs were calculated (Tables 2, 3, 4).

As expected, the objective noise of the FBP image decreased as the dose increased (Fig. 4). At 10–40 mAs,

Table 2 Subjective quality scores for noise

Image	SQS (mean ± SD)	Comparison by Tukey's HSD									
		A_0	A_{20}	A_{40}	B_0	B_{20}	B_{40}	C_0	C_{20}	C_{40}	D_0
A_0	−1.12 ± 0.10	–									
A_{20}	−0.88 ± 0.08	NS	–								
A_{40}	−0.55 ± 0.13	**	**	–							
B_0	−0.29 ± 0.07	**	**	*	–						
B_{20}	0.00 ± 0.10	**	**	**	*	–					
B_{40}	0.30 ± 0.06	**	**	**	**	*	–				
C_0	0.33 ± 0.03	**	**	**	**	**	NS	–			
C_{20}	0.65 ± 0.04	**	**	**	**	**	**	**	–		
C_{40}	0.70 ± 0.09	**	**	**	**	**	**	**	NS	–	
D_0	0.87 ± 0.12	**	**	**	**	**	**	**	NS	NS	–

Image labels are defined in Table 1

SQS subjective quality score, *SD* standard deviation, *Tukey's HSD* Tukey's honestly significant differences test

NS $P \geq 0.05$, * $P < 0.05$, ** $P < 0.01$

Table 3 Subjective quality scores for sharpness

Image	SQS (mean ± SD)	Comparison by Tukey's HSD									
		A_0	A_{20}	A_{40}	B_0	B_{20}	B_{40}	C_0	C_{20}	C_{40}	D_0
A_0	−0.99 ± 0.23	–									
A_{20}	−0.90 ± 0.08	NS	–								
A_{40}	−0.75 ± 0.05	NS	NS	–							
B_0	−0.12 ± 0.29	**	**	**	–						
B_{20}	0.05 ± 0.15	**	**	**	NS	–					
B_{40}	0.30 ± 0.09	**	**	**	NS	NS	–				
C_0	0.43 ± 0.09	**	**	**	*	NS	NS	–			
C_{20}	0.54 ± 0.07	**	**	**	**	NS	NS	NS	–		
C_{40}	0.73 ± 0.20	**	**	**	**	**	NS	NS	NS	–	
D_0	0.72 ± 0.26	**	**	**	**	**	NS	NS	NS	NS	–

Image labels are defined in Table 1

SQS subjective quality score, *SD* standard deviation, *Tukey's HSD* Tukey's honestly significant differences test

NS $P \geq 0.05$, * $P < 0.05$, ** $P < 0.01$

Table 4 Subjective quality scores for nodules

Image	SQS (mean ± SD)	Comparison by Tukey's HSD									
		A_0	A_{20}	A_{40}	B_0	B_{20}	B_{40}	C_0	C_{20}	C_{40}	D_0
A_0	−1.07 ± 0.12	–									
A_{20}	−0.90 ± 0.14	NS	–								
A_{40}	−0.76 ± 0.12	NS	NS	–							
B_0	−0.01 ± 0.09	**	**	**	–						
B_{20}	0.25 ± 0.10	**	**	**	NS	–					
B_{40}	0.48 ± 0.01	**	**	**	*	NS	–				
C_0	0.25 ± 0.14	**	**	**	NS	NS	NS	–			
C_{20}	0.52 ± 0.06	**	**	**	**	NS	NS	NS	–		
C_{40}	0.41 ± 0.34	**	**	**	*	NS	NS	NS	NS	–	
D_0	0.83 ± 0.01	**	**	**	**	**	NS	**	NS	*	–

Image labels are defined in Table 1

SQS subjective quality score, *SD* standard deviation, *Tukey's HSD* Tukey's honestly significant differences test

NS $P \geq 0.05$, * $P < 0.05$, ** $P < 0.01$

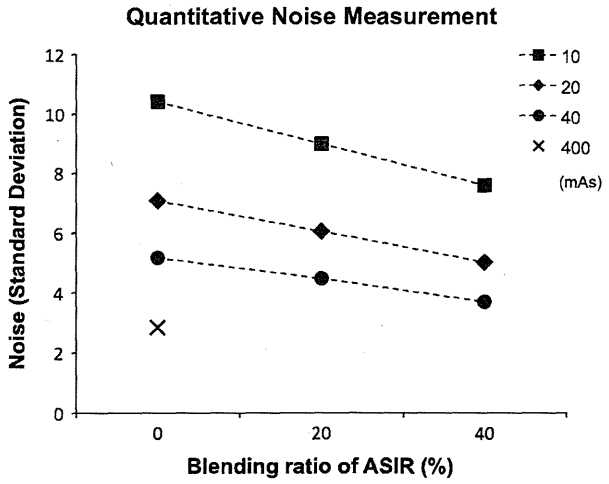

Fig. 4 Objective image noise measured as the standard deviation of attenuation values is plotted against blending ratio of ASIR. As expected, objective noise of 0%-ASIR image (FBP image) decreases as dose increases. At 10–40 mAs, image noise decreases almost linearly as the percentage of ASIR increases

objective noise decreased almost linearly as the percentage of ASIR increased, which is consistent with the result of a previous study [9].

SQSs are plotted against quantitative noise data in Fig. 5. In general, both SQS and image SD were improved with increasing the scan dose and the blending ratio of ASIR. The correlation between the mean SQS and image SD was good (Pearson's correlation coefficient: $r = -0.991$ for noise, −0.967 for sharpness and −0.953 for nodule, respectively).

At all doses, applying 40% ASIR to an FBP image increased the SQS for noise significantly ($P < 0.01$, at all doses). Applying 40% ASIR to an FBP image also increased the SQSs for image sharpness and conspicuity of tiny nodules, but these increases were generally not significant. A half dose 40%-ASIR image (B_{40}) had a slightly smaller SD value than the standard dose FBP image (C_0) (5.0 vs. 5.2) and was comparable in terms of SQSs (0.30 vs. 0.33, $P = 1.000$ for noise; 0.30 vs. 0.43, $P = 0.993$ for sharpness; 0.48 vs. 0.25, $P = 0.653$ for nodules). A quarter dose 40%-ASIR image (A_{40}) had a slightly higher SD value than the half dose FBP image (B_0) (7.6 vs. 7.1) and was significantly worse than the image B_0 in terms of SQSs (−0.55 vs. −0.29, $P = 0.038$ for noise; −0.75 vs. −0.12, $P = 0.007$ for sharpness; −0.76 vs. −0.01, $P < 0.001$ for nodules).

Discussion

On assessment of image quality, objective analysis is considered to be superior to subjective analysis in terms of accuracy and reproducibility of the result and suitable for strict quality assessment of technologies or products. For quality check of clinical images, however, assessment by the expert in medical imaging is still necessary at the present time because no objective measurements give a precise enough prediction of perceived image quality for the expert to abandon the subjective analysis. In the present study, a method based on Anderson's functional measurement theory was applied for the subjective analysis. Presenting images as a pair, by placing images side by side or toggling between two images by user operation [15], helps readers to evaluate the superiority or inferiority of images in more detail than presenting images separately. Presentation of image pairs is also utilized in the double-stimulus continuous-quality scale (DSCQS) method, which is a

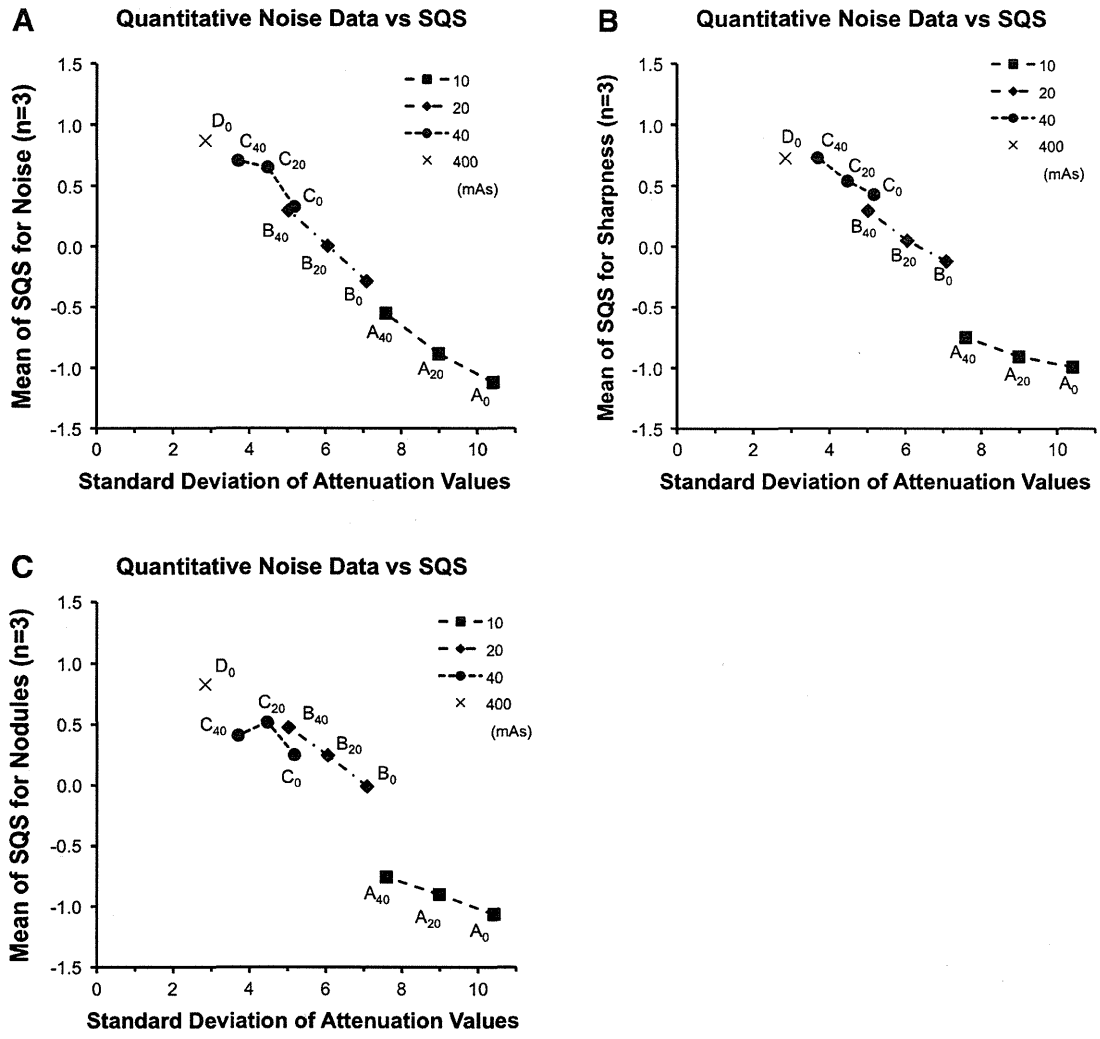

Fig. 5 The mean of the subjective quality score (*SQS*) is plotted against the standard deviation of attenuation (image SD). The correlation between the mean of SQS and the image SD is relatively good (Pearson's coefficient of correlation: $r = -0.991$ for noise, -0.967 for sharpness, and -0.953 for nodules). Image A_{40} had a higher SD value than image B_0 (7.6 vs. 7.1, respectively) and significantly lower SQSs than image B_0 (-0.55 vs. -0.29, $P = 0.038$ for noise; -0.75 vs. -0.12, $P = 0.007$ for sharpness and -0.76 vs. -0.01, $P < 0.001$ for nodules, respectively). **a** Noise, **b** sharpness, **c** nodules

popular method for assessment of image quality in the field of broadcasting proposed by the International Telecommunication Union. Use of a scale with at least ten steps is recommended by functional measurement theory [14]. A psychological study reported that, irrespective of popular use, a five-point scale was not optimal and more response categories appeared better with regard to reliability, validity and discriminating power [16]. We think the method in the present study was likely to evaluate superiority and inferiority of image quality more sensitively and reliably than conventional five-step rating.

In the present study, a 40%-ASIR image obtained at half dose generally had comparable image quality to the standard-dose FBP image. The 40%-ASIR images obtained at the quarter dose were worse than half-dose FBP images with regard to both the image SD and subjective score. According to the trend seen in Fig. 3, it may be difficult to improve subjective image quality of the quarter dose image to the level of the half-dose FBP image. These results may imply that using ASIR cannot compensate for the degradation of quality of a reduced-dose image at a lower range of scan doses as well as at a standard range. If a low-dose scan protocol for clinical lung imaging had already been used, considerable dose reduction would not have been achievable using ASIR.

In the present study, fairly good linear correlation was observed between the subjective score and the objective measurement for image noise. Although ASIR changes

noise texture [4, 6], the change had less effect on the perceived amount of image noise. Relatively good correlation was also observed between the SQS and the image SD with regard to sharpness and visualization of tiny nodules. The image SD may be used as a rough predictor of subjective image quality as long as the dose reduction is less than 50%.

This study had limitations. Since no human images were assessed, results of this study may not directly apply to clinical imaging. The assumed standard dose for porcine lungs may not simulate a standard dose of clinical lung imaging as well. Use of a slice thickness of 5 mm is another major limitation of this study. Smaller slice thicknesses are currently used in clinical chest imaging, and many normal and abnormal findings on chest CT are visualized suboptimally on 5-mm slices. This may significantly affect the result particularly for the evaluation of approximately 1-mm peripheral nodules. Another limitation is that a reconstruction kernel that emphasizes a high frequency component was not used. With such a kernel, image noise would increase, and use of ASIR might be more effective. Experiments with a thinner slice and a kernel emphasizing high frequency would be more suitable for considering the quality of ASIR images for lung CT. Lesions with ground-glass opacity including bronchioloalveolar carcinoma and interstitial pneumonia were not evaluated, nor were low attenuating areas present in emphysema. Images with an ASIR level of more than 40% were not evaluated. A higher degree of ASIR would be beneficial for dose reduction in some clinical situations like screening. A recent article using clinical images reported that images reconstructed with a higher percentage of ASIR (70%) had a blothy pixilated texture, which did not affect the diagnostic confidence [17]. Application of Anderson's functional measurement theory in medical research is not common, and the reproducibility of the result was not tested.

In conclusion, compared to the FBP algorithm, ASIR for lung CT may enable an approximately 50% reduction in dose from the standard dose, and visualization of small structures is preserved.

Acknowledgments None.

References

1. Mettler FA Jr, Bhargavan M, Faulkner K, Gilley DB, Gray JE, Ibbott GS, et al. Radiologic and nuclear medicine studies in the United States and worldwide: frequency, radiation dose, and comparison with other radiation sources—1950–2007. Radiology. 2009;253:520–31.
2. Berrington de Gonzalez A, Darby S. Risk of cancer from diagnostic X-rays: estimates for the UK and 14 other countries. Lancet. 2004;363:345–51.
3. Kubo T, Lin PJ, Stiller W, Takahashi M, Kauczor HU, Ohno Y, et al. Radiation dose reduction in chest CT: a review. AJR Am J Roentgenol. 2008;190:335–43.
4. Marin D, Nelson RC, Schindera ST, Richard S, Youngblood RS, Yoshizumi TT, et al. Low-tube-voltage, high-tube-current multidetector abdominal CT: improved image quality and decreased radiation dose with adaptive statistical iterative reconstruction algorithm—initial clinical experience. Radiology. 2010;254:145–53.
5. Pontana F, Duhamel A, Pagniez J, Flohr T, Faivre JB, Hachulla AL, et al. Chest computed tomography using iterative reconstruction vs filtered back projection (part 2): image quality of low-dose CT examinations in 80 patients. Eur Radiol. 2011;21:636–43.
6. Prakash P, Kalra MK, Digumarthy SR, Hsieh J, Pien H, Singh S, et al. Radiation dose reduction with chest computed tomography using adaptive statistical iterative reconstruction technique: initial experience. J Comput Assist Tomogr. 2010;34:40–5.
7. Yanagawa M, Honda O, Yoshida S, Kikuyama A, Inoue A, Sumikawa H, et al. Adaptive statistical iterative reconstruction technique for pulmonary CT: image quality of the cadaveric lung on standard- and reduced-dose CT. Acad Radiol. 2010;17:1259–66.
8. Leipsic J, Nguyen G, Brown J, Sin D, Mayo JR. A prospective evaluation of dose reduction and image quality in chest CT using adaptive statistical iterative reconstruction. AJR Am J Roentgenol. 2010;195:1095–9.
9. Hara AK, Paden RG, Silva AC, Kujak JL, Lawder HJ, Pavlicek W. Iterative reconstruction technique for reducing body radiation dose at CT: feasibility study. AJR Am J Roentgenol. 2009;193:764–71.
10. van Dijk AM, Martens JB. Subjective quality assessment of compressed images. Signal Process. 1997;58:235–52.
11. Miao J, Huo D, Wilson DL. Quantitative image quality evaluation of MR images using perceptual difference models. Med Phys. 2008;35:2541–53.
12. Escalante-Ramírez B, Martens J, de Ridder H. Multidimensional characterization of the perceptual quality of noise-reduced computed tomography images. J Vis Commun Image Represent. 1995;6:317–34.
13. Markarian B, Dailey ET. Preparation of inflated lung specimens. In: Heizman ER, editor. The lung: radiologic-pathologic correlations. 2nd ed. Mosby: St. Louis; 1984. p. 4–12.
14. Anderson NH. Algebraic models in perception. In: Carterette EC, Friedman MP, editors. Handbook of perception: volume 2, psychophysical judgment and measurement. 1st ed. New York: Academic Press; 1974. p. 215–98.
15. Slone RM, Foos DH, Whiting BR, Muka E, Rubin DA, Pilgram TK, et al. Assessment of visually lossless irreversible image compression: comparison of three methods by using an image-comparison workstation. Radiology. 2000;215:543–53.
16. Preston CC, Colman AM. Optimal number of response categories in rating scales: reliability, validity, discriminating power, and respondent preferences. Acta Psychol. 2000;104:1–15.
17. Singh S, Kalra MK, Gilman MD, Hsieh J, Pien HH, Digumarthy SR, et al. Adaptive statistical iterative reconstruction technique for radiation dose reduction in chest CT: a pilot study. Radiology. 2011;259:565–73.

Int J Cardiovasc Imaging (2012) 28:139–146
DOI 10.1007/s10554-010-9759-0

ORIGINAL PAPER

Relationship between beat to beat coronary artery motion and image quality in prospectively ECG-gated two heart beat 320-detector row coronary CT angiography

Nobuo Tomizawa · Shuhei Komatsu · Masaaki Akahane · Rumiko Torigoe · Shigeru Kiryu · Kuni Ohtomo

Received: 25 September 2010 / Accepted: 19 November 2010 / Published online: 30 November 2010

Abstract The objective was to investigate the influence of the beat-to-beat movement of the coronary arteries on image quality of multi-segment reconstruction (MSR) images. Although MSR improves temporal resolution, image quality would be degraded by beat-to-beat movement of the coronary arteries. In a retrospectively review, 18 patients (mean age, 67.0 years) who underwent coronary CT angiography using a 320-detector row CT were included. The displacement and diameter of coronary artery segments for each of the identified nine landmarks was recorded. The motion ratio was calculated as the division of displacement by diameter. Image quality (IQ) was graded by a four-point scale. The correlation between MSR IQ score and the motion ratio showed stronger negative correlation than that between MSR IQ score and the displacement ($r = -0.54$ vs. $r = -0.36$). The average motion ratio for segments in which half-scan reconstruction (HSR) IQ was better than MSR IQ (29.1%, group A) was higher than that for segments in which MSR IQ was better than HSR IQ (16.0%, group C). The motion ratio in group C was lower than 25%. Difference in IQ scores of the HSR images was more frequent in group A than in the remaining segments in which the motion ratio was lower than 25% (16.7% vs. 66.0%; $P < 0.0002$). The motion ratio could be a better index than the displacement to evaluate the influence of the motion of coronary arteries on image quality. MSR images would be impaired by a motion ratio larger than 25%. Image impairment of one of the HSR images might also impair MSR images.

Keywords Coronary CT angiography · Half-scan reconstruction · Image quality · Multi-segment reconstruction · Movement of coronary artery

N. Tomizawa (✉) · S. Komatsu · M. Akahane · K. Ohtomo
Department of Radiology, The University of Tokyo, 7-3-1 Hongo, 113-0033 Bunkyo-ku, Tokyo, Japan
e-mail: tomizawa-tky@umin.ac.jp

R. Torigoe
Toshiba Medical Systems Corporation, Tokyo Metropolitan Regional Office, 1-6 Tsukuda 2-Chome, 104-0051 Chuo-ku, Tokyo, Japan

S. Kiryu
Department of Radiology, Institute of Medical Science, The University of Tokyo, 4-6-1 Shirokanedai, 108-8639 Minato-ku, Tokyo, Japan

Introduction

Advances in computed tomography (CT) have improved image quality, leading to increased accuracy of diagnosis of coronary artery disease. Coronary CT angiography (CCTA) is indicated in several clinical pathologies due to its high negative predictive value [1–5]. The wide area of the detector in 320-detector row CT has enabled whole heart coverage in an axial (not helical) scan mode with one gantry